Structural studies of magnetic C_{60}/Cu multilayers

J. E. Shoup, D. A. Arena, J. A. Borchers, B. J. Kirby, A. J. Caruana (iD), C. J. Kinane, S. Langridge, M. Rogers (iD), and O. Cespedes (iD)

View Online   Export Citation   CrossMark

ARTICLES YOU MAY BE INTERESTED IN

PNR study of the phase transition in FeRh thin films
APL Materials **7**, 101117 (2019); https://doi.org/10.1063/1.5120622

Superconductivity-driven negative interfacial magnetization in $YBa_2Cu_3O_{7-\delta}$/$SrTiO_3$/$La_{0.67}Sr_{0.33}MnO_3$ heterostructures
Applied Physics Letters **116**, 022406 (2020); https://doi.org/10.1063/1.5135578

Ultrathin interfacial layer with suppressed room temperature magnetization in magnesium aluminum ferrite thin films
Applied Physics Letters **115**, 132404 (2019); https://doi.org/10.1063/1.5111326

Structural studies of magnetic C_{60}/Cu multilayers

View Online   Export Citation   CrossMark

J. E. Shoup,[1] D. A. Arena,[1,a)] J. A. Borchers,[2] B. J. Kirby,[2] A. J. Caruana,[3] C. J. Kinane,[3] S. Langridge,[3]
M. Rogers,[4] and O. Cespedes[4]

AFFILIATIONS

[1] Department of Physics, University of South Florida, Tampa, Florida 33620, USA
[2] NIST Center for Neutron Research, NIST, Gaithersburg, Maryland 20899, USA
[3] ISIS Neutron and Muon Source - Didcot, Oxfordshire OX11 0QX, United Kingdom
[4] School of Physics and Astronomy, University of Leeds, Leeds LS2 9JT, United Kingdom

[a)] Author to whom correspondence should be addressed: darena@usf.edu

ABSTRACT

We report on x-ray and neutron scattering studies that reveal the structure of interfaces of C_{60} layers with adjacent transition metal layers, in this instance, Cu. Such interfaces produce room-temperature long-range spin order that is not described by conventional theories of metallic magnetism. We use a combination of hard x-ray reflectivity and neutron scattering to investigate the interfacial structure of two C_{60}/Cu layered samples: a superlattice with multiple C_{60}/Cu repeats and a simpler tri-layer structure. For both structures, we develop a consistent structural model for the two scattering techniques, which details the critical interfacial roughness between the layers. We find that while x-ray reflectivity provides a strong contrast between the C_{60} and Cu layers, the similar neutron scattering length density of the two materials severely reduces the neutron scattering contrast. Our results can be used to design material systems that permit studies of the magnetism of the C_{60}/transition metal interfaces with spin-sensitive scattering probes such as polarized neutron reflectometry.

INTRODUCTION

Molecular spintronics has a fundamental appeal and also offers the promise of practical applications as the incorporation of active organic components into device structures presents an unparalleled variation of device functionality. The flexibility of physical parameters (e.g., transport properties, luminescence, and chemical sensitivity) afforded by molecular active layers[1,2] supports development of new device concepts such as spin-sensitive organic light emitting diodes.[3] With specific regard to spin applications, organic components possess additional desirable properties such as both a large spin diffusion length and long spin lifetime.[4,5] These and other characteristics motivate the search for all-organic or hybrid organic/inorganic structures that may form the platform for realizing room-temperature quantum coherent spin manipulation.

Among the molecular species, the C_{60} fullerene molecule is noteworthy. As in many other organic molecules, electron transport in C_{60} is primarily via electron hopping,[6] which reduces Eliot–Yafet type spin depolarization. Spin-orbit coupling (SOC) is also weak in

C_{60}, and the molecule has a saturated, all-carbon bond network without any hydrogen. These characteristics result in low contributions to spin dephasing and spin memory loss from SOC and hyperfine interactions.[4] These effects support long spin diffusion paths in C_{60}, and the material can be used to examine non-local spin interactions such as spin-pumping.[7] C_{60} is also an efficient electron acceptor that can produce significant changes to the electronic structure of C_{60}/metal interfaces.[8] Such attractive features of C_{60} for spintronics have been explored in devices such as spin valves where a robust room-temperature magneto-resistance has been reported in hybrid Co/C_{60}/Al-oxide/Fe_3O_4 spin valves.[9]

One of the most unexpected spin-related properties of C_{60} heretofore reported is the emergence of room-temperature long-range spin ordering in multilayer films of C_{60} and non-ferromagnetic transition metals such as Cu or Mn.[10] The magnetism in these systems is clearly interfacial in origin as the effect scales with the number of interfaces and the interfacial magnetization is roughly four times larger in C_{60}/Cu films than C_{60}/Mn. Thin film C_{60} forms a van der Waals bonded fcc lattice with a relatively poor lattice parameter that matches with the adjacent metal film.

Therefore, new details on the C_{60}/Cu interface will enhance the understanding of the unusual magnetism in these materials.

The phenomenon of room-temperature magnetism originating from the interfaces of non-ferromagnetic materials has been observed in inorganic metallic/semiconducting interfaces, where band alignment, charge transfer, and local polaronic lattice distortions can produce a charge density enhancement in the interfacial region that is associated with emergence of ferromagnetism.[11] Unusual magnetic effects are also observed in C_{60}/ferromagnetic interfaces that are closely associated with the local atomic and electronic structure either observed or calculated for the interface. For example, the orbital hybridization and associated charge transfer of C_{60} on Fe(001) lead to the development of a magnetic moment of ~ 0.2–0.25 μ_B per C_{60} molecule that is oriented anti-parallel to the net Fe moment. On the other side of the interface, the Fe moments are reduced by ~6% as experimentally determined by x-ray spectroscopy that averages over the entire C_{60}/Fe interface as well as the near-surface Fe, although computational studies suggest that the local moment reduction may be much larger for Fe atoms at the surface in direct contact with C_{60}.[12]

C_{60}/metal interfaces are, thus, seen to lead to a number of effects that modify emergent ferromagnetism, and to better understand the nature of such interfaces, we have conducted a series of detailed structural studies of C_{60}/Cu multilayer samples. We utilize a combination of x-ray and neutron scattering techniques to investigate the evolution of the interfaces between the organic molecule and the transition metal in two types of structures: C_{60}/Cu superlattices designed to maximize the total magnetic moment and trilayer structures that highlight the role of a single interface.

METHODS

We conducted extensive structural studies on two samples; the substrates for both were Si wafers with a SiO_x layer on top. The superlattice (SL) sample has a structure with repeated C_{60}/Cu layers: substrate/(C_{60} [100]/Cu [25])$_{\times 5}$/Al[80] (brackets denote thickness in Å). The SiO_x layer for the SL sample is a thermally grown oxide layer and is ~1000 Å thick. The tri-layer (TL) sample has a relatively simple structure of $C_{60}/Cu/C_{60}$ with nominal values of substrate/Ta [25]/C_{60} [100]/Cu [35]/C_{60} [100]/Au [100]. In addition, we examined a third sample (TL 2) with the same basic structure as the tri-layer sample but with double the C_{60} thickness: substrate/Ta [25]/C_{60} [200]/Cu [35]/C_{60} [200]/Au [100]. The SiO_x layers for both

TL samples are a native oxide and are ~30 Å thick. Nominal thickness values were determined from calibration runs of the multi-layer constituents. Relatively thick capping layers were used in all the samples to minimize oxidation of the transition metal films and to preserve the critical transition metal/C_{60} interface. The first few dozen Å of the cap layers were grown at low power to minimize diffusion of the cap and the C_{60} layers. Deposition rates for the cap layer were then increased to complete the structure. This may result in a variation of the cap layer density. Metallic layers were deposited via DC magnetron sputtering, while the C_{60} films were deposited via thermal evaporation. Magnetic properties of the films are determined using a superconducting quantum interference device operated as a vibrating sample magnetometer (SQUID-VSM); the sensitivity of the instrument is better than 10^{-11} Am^2 (10^{-8} emu).

A combination of x-ray and neutron scattering was used to obtain a structural profile of the samples. Low angle x-ray reflectivity (XRR) scans were conducted with a high-resolution x-ray diffraction system using Cu $K - \alpha$ radiation and across an angular range of 0°–~6°. High angle x-ray diffraction scans were acquired with a four-circle high-resolution laboratory x-ray diffraction instrument. Neutron reflectivity (NR) scans were acquired at two different facilities: the polarized beam reflectivity (PBR) instrument at the NIST Center for Neutron Research (NCNR) in Gaithersburg, MD, USA, and at the PolRef beam line of the ISIS Neutron and Muon Source in Didcot, UK. Neutron reflectivity scans from the SL sample were recorded at the PBR instrument, which operates on a fixed wavelength of 4.75 Å, and cold neutron guide and reflectivity scans are acquired by varying the incident angle of the neutrons while maintaining the specular reflection condition (standard $\theta - 2\theta$ configuration).[13] We used the PolRef instrument to examine the TL sample; PolRef operates at the ISIS spallation neutron source, which is well-suited for time-of-flight measurements with a distribution of neutron wavelengths and a fixed incident angle on the sample.[14]

MEASUREMENTS, MODELING AND RESULTS

As in earlier studies,[10] both the SL and TL samples exhibited long-range magnetic ordering originating from the C_{60}/Cu interfaces. Full field hysteresis loops were measured on both samples, and a half-loop was repeated for the SL sample immediately prior to the neutron scattering measurements [see Fig. 1(a)]. The saturation magnetization of the SL sample was ~$5 \cdot 10^{-9}$ Am^2 ($5 \cdot 10^{-6}$ emu),
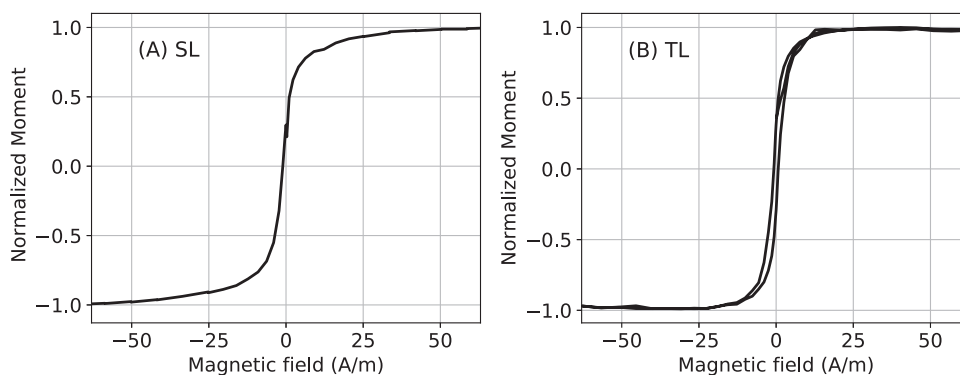
FIG. 1. Field hysteresis curves for the superlattice [SL, panel (a)] and tri-layer [TL, panel (b)] samples, normalized to the saturation moment. The SL data are a half-loop acquired just prior to the neutron measurements. The average interfacial moment per unit area is $2.3 \cdot 10^{-9}$ J/T cm^2 ($2.3 \cdot 10^{-6}$ emu/cm^2) for the SL sample and $2.4 \cdot 10^{-10}$ J/T cm^2 ($2.4 \cdot 10^{-7}$ emu/cm^2) for the TL sample. Both samples exhibit a remanence ratio of ~2.7–3.

which translates to a moment per interface per unit area of approximately $2.3 \cdot 10^{-9}$ J/T cm^2 ($2.3 \cdot 10^{-6}$ emu/cm^2) [Fig. 1(a)]. The simpler TL structure exhibited a smaller magnetic signal of around $1.1 \cdot 10^{-9}$ Am^2 ($1.1 \cdot 10^{-6}$ emu) which results in an average interfacial moment of about $2.4 \cdot 10^{-10}$ J/T cm^2 ($2.4 \cdot 10^{-7}$ emu/cm^2) [Fig. 1(b)]. The remanence ratio of 2.7–3 is similar for both samples.

Having verified the spin order of these samples, we investigated the bulk and interfacial structures using multiple techniques. High angle x-ray diffraction (XRD) is useful for retrieving the crystal structure/symmetry of the sample layers. Low angle XRR and NR are both used to probe the structure of the individual layers; i.e., thickness, roughness, and x-ray and neutron scattering length densities (SLD). By using an incident neutron beam with polarized spins and analyzing the spins of the reflected beam, additional details on the magnetic depth profile can be extracted (polarized neutron reflectometry or PNR); however, in samples with weak magnetization, both NR and PNR are almost completely dominated by scattering from the sample structure.[15]

The thicker C_{60} layers in the tri-layer 2 (TL2) sample permitted determination of high angle diffraction patterns from the molecular carbon layer. Scattering from the molecular film was weak, but a clearly defined C_{60} peak can be resolved. Figure 2 shows a weak low angle XRD peak at ∼11° from the C_{60} layers in the sample that indexes to the (111) reflection of a close-packed, face centered cubic type structure with a lattice parameter of $a_{C60} \sim 14$ Å. Similar values have been reported for C_{60} powders and thermally evaporated films.[16] The diffraction peak width suggests a grain size of about 160 Å for the 200 Å C_{60} films. The high angle XRD, thus, indicates
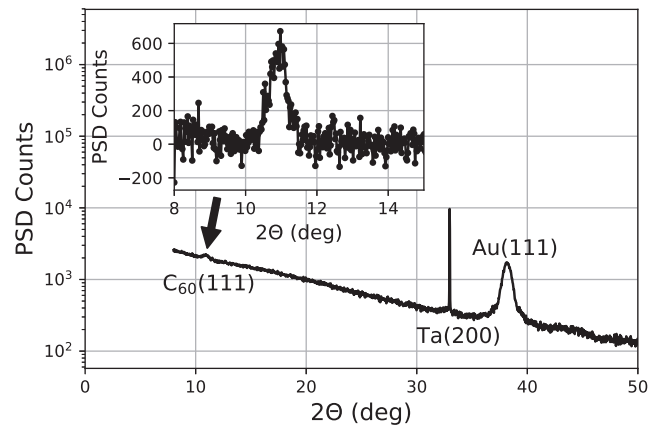
FIG. 2. High angle, out-of-plane XRD showing the C_{60} (111) peak at ∼11°, Ta (200) at ∼33°, and Au(111) at ∼38°. Inset: expanded scale around the C_{60}(111) peak. The grain size derived from the C_{60} peak width is about 160 Å.

that the C_{60} molecules form a large-grain close-packed cubic structure but with an incommensurate lattice match to the adjacent Cu layers ($a_{Cu} \sim 3.61$ Å).

The interfacial structure of the samples was investigated using a combination of low angle x-ray (XRR) and neutron reflectivity (NR). Figure 3 presents the results for the TL and SL samples in black. The XRR and NR data were modeled with the Refl1D specular
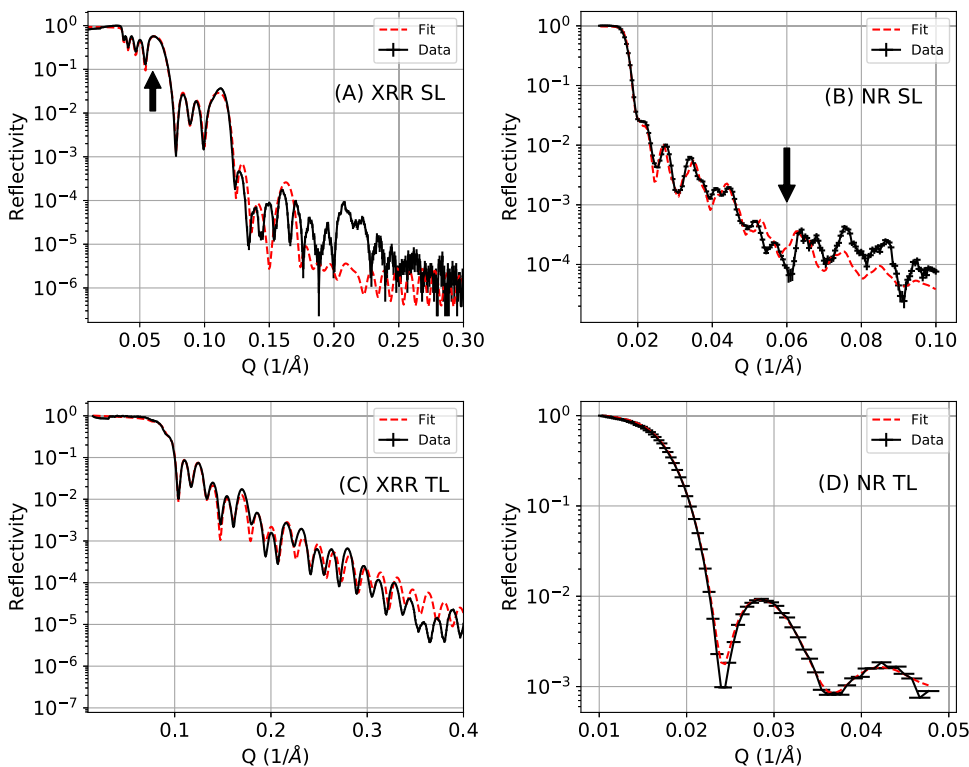
FIG. 3. [(a) and (b)] XRR and NR scans for the SL samples. Superlattice Bragg peaks are visible at $Q \sim 0.06$, 0.11, and 0.22 Å^{-1} in the XRR data but are not present at $Q \sim 0.06$ Å^{-1} in the NR data. [(c) and (d)] XRR and NR data and fits for the TL sample. Black lines are the scattering data; red dashed lines are best fit models. See text for details.

TABLE I. Structural parameters for the SL sample used in the models presented in Fig. 3. The bold lines indicate the C_{60}/Cu layers repeated four times in the model. The values for the roughness of layer n are for the interface of that layer and the layer above it (i.e., the roughness listed for Si refers to the Si/SiO$_2$ interface).

Layer	X-ray thickness (Å)	X-ray roughness (Å)	X-ray SLD(10^{-6}/Å)	Neutron thickness (Å)	Neutron roughness (Å)	Neutron SLD(10^{-6}/Å)
Al$_2$O$_3$	39	23	35.8	39	35	6.0
Al	33	20	22.4	47	45	3.7
Cu$_{top}$	39	15	61.8	32	12	2.4
C$_{60top}$	113	25	13.7	91	15	5.3
Cu$_{R4}$	34	13	63.4	38	13	5.6
C$_{60,R4}$	85	13	13.4	80	13	5.4
SiO$_2$	1182	2	18.8	1348	12	3.5
Si	n/a	19	20.0	n/a	14	2.1

reflectivity modeling software;[17] the best fit models are shown as red dashed lines and discussed below. Fit parameters for the structural models are presented in Tables I and II; the 1-sigma estimated uncertainties in the structural parameters are less than 10%. The structural parameters and confidence intervals are highly dependent on constraints used in our structural models, and we discuss some of these dependencies below.

The XRR data for the SL structure were acquired over a Q-range of 0.007–0.4 Å^{-1} [Fig. 3(a)]. The XRR data show high frequency Kiessig fringes reflecting the total thickness of the SL structure as well as prominent superlattice Bragg peaks at $Q \sim 0.06$ Å^{-1} and 0.11 Å^{-1} and a weaker feature at 0.22 Å^{-1}. The NR for the SL sample over the Q-range of 0.01–0.1 Å^{-1} was collected at the NIST-PBR instrument, and these data are presented in Fig. 3(b). The high frequency Kiessig fringes are also apparent in the NR data. However, the expected superlattice Bragg peak at $Q \sim 0.06$ Å^{-1} is absent, which may be due to differences in the sampling volume between x-ray and neutron measurements (primarily due to differences in beam width), the variation in SLD of the materials, or interfacial roughness.

Figures 3(c) and 3(d) present similar XRR and NR scans for the TL sample. In comparing the TL to the SL sample, several features stand out. First, the critical edges for the XRR scans are very different for the two samples, reflecting the different cap layers deposited (Al for the SL and Au for the TL). However, the critical edge

TABLE II. Structural parameters for the TL from the common fit of both NR and XRR.

Layer	Thickness (Å)	Roughness (Å)	X-ray SLD(10^{-6}/Å)	Neutron SLD(10^{-6}/Å)
Au	59	4	152.5	2.8
Au, L2	49	6	153.6	5.2
C$_{60}$	102	11	23.8	4.8
Cu	50	5	55.9	6.3
C$_{60}$, L2	85	6	23.8	5.2
Ta	32	15	112.2	4.8
SiO$_2$	35	5	20.2	4.1
Si	n/a	6	20.2	2.1

for the NR of the TL is almost indistinguishable from that of the SL ($Q \sim 0.016$ Å^{-1}) despite the different capping layers. As the TL sample has a considerably simpler profile than the SL, prominent Kiessig fringes dominate the scan, modulated by Q-dependent interference effects. Only two Kiessig fringes in the NR [Fig. 3(d)] at $Q \sim 0.029$ Å^{-1} and 0.042 Å^{-1} are visible, reflecting the much narrower range used for the NR measurements at the PolRef instrument.
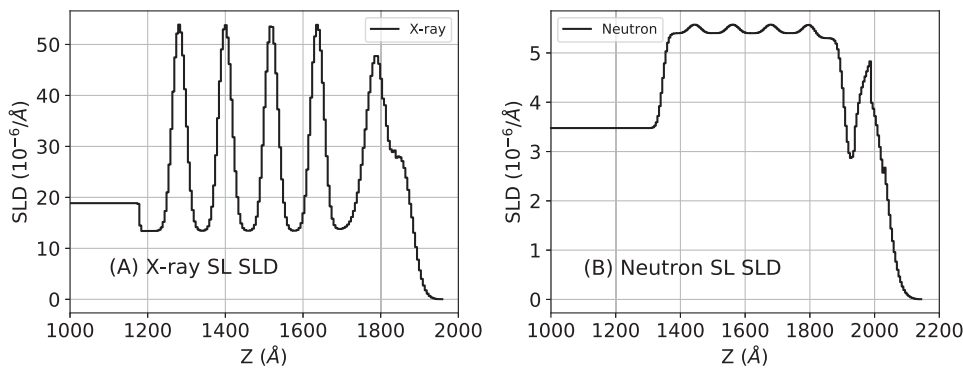
The analysis of the SL was complicated by the large number of individual layers in the sample. Modeling and fitting of the full structure resulted in unphysical values for the structural and material parameters; however, a pattern emerged in the modeling, suggesting a larger variation in the thickness and roughness of the top C_{60} and Cu layers, while the interfacial roughness of the $C_{60} \rightarrow$ Cu and Cu $\rightarrow C_{60}$ interfaces for the lower four repeated layers appeared similar. Hence, to reduce the number of free parameters in the final model, we constrained it by requiring the parameters of the model for the bottom 4 repeats of the (C_{60}/Cu) double layer to be identical. However, the fit parameters of the top C_{60} and Cu layers were free to vary. Even with the simplified model, it was difficult to obtain a satisfactory fit for both the XRR and NR using a single set of parameters. Individual fits of the XRR and NR resulted in small variations of thickness and roughness for the different layers. The modeling of the x-ray and neutron reflectivities also indicated that the cap layer for the SL sample was not a monolithic Al slab. Recalling that the Al cap was deposited in two steps (low power/high power), we modeled the cap layer as a slab of metallic Al with a layer of Al-oxide (Al$_2$O$_3$) on top. Simulations that implemented two Al layers with different densities did not reproduce the data well.

The results of the structural model for the SL are presented in Figs. 3(a) and 3(b) as red dashed lines, while the resulting SLD profile can be seen in Fig. 4. Numerical fit values are presented in Table I, and the calculated SLD of the different materials in the superlattice are generally within ~10% of the tabulated values. The agreement between the XRR and NR models is reasonable. The XRR model reproduces the first two superlattice Bragg peaks at $Q \sim 0.06$ and 0.11 Å^{-1} but suggests that a weaker Bragg peak should appear at $Q \sim 0.16$ Å^{-1} and does not reproduce the XRR peak at $Q \sim 0.22$ Å^{-1}. These limitations may arise from the model constraint that requires identical structural parameters for the bottom four

FIG. 4. Modeled SLD profiles of the SL structure for the XRR (a) and NR (b). The contrast of the SLDs between Cu and C_{60} is strong for the x-rays (a) while much weaker for the neutrons (b).

C_{60}/Cu repeats. Small lateral variations in layer structure whose scattering sums incoherently may reduce the superlattice Bragg peaks in the NR dataset. The thickness of the top C_{60} layer increases by ~10%–30%. The XRR model exhibits a strong increase in the roughness of the top $C_{60} \rightarrow$ Cu interface, while the NR shows a negligible increase in roughness. However, the NR model also indicates a reduction of the top Cu SLD, which may compensate for the decreased roughness. In general, the modeling indicates that the top C_{60}/Cu layer shows a considerable variation in structure from the layers closer to the substrate, and this variation takes the form of an increase in interface roughness and/or a decrease in density. The roughness in the top C_{60}/Cu layers propagates into the Al/Al_2O_3 cap layers. The NR model, in particular, suggests that the roughness of the Al/Al_2O_3 cap layers is of the same order as the layer thickness, which may indicate that the layers are fully interdiffused.

By examining the SLD profile for the SL in Fig. 4, the origin of the missing superlattice Bragg peak in the NR [black arrow in Fig. 3(b)] becomes clear. While the x-ray scattering factors for Cu and C_{60} produce intense variations in SLD, the contrast of the SLDs is much weaker for the neutrons. Hence, the interference effects that support the enhanced scattering intensity at the superlattice Bragg peak positions are weaker and the influence of interface roughness washes out most of the expected increased scattering at those Q-values.

Turning to the TL sample, the Q-range of the XRR was much larger than the NR (up to 0.4 Å^{-1} for the XRR and up to 0.045 Å^{-1} for the NR). Therefore, we used the XRR to model the main structural parameters of the sample. We fixed the thickness and roughness values when fitting the NR SLD and were able to develop a consistent structural model between the two datasets. The modeled reflectivity profiles are presented as red dashed traces in Figs. 3(c) and 3(d), while the extracted structural parameters and SLDs are presented in Table II.

The layer thickness values from the optimized model are generally in agreement with the nominal values from the growth run. However, the interfaces between the layers exhibit considerable variation. In particular, the Ta $\rightarrow C_{60}$ and the $C_{60} \rightarrow$ Au interfaces have a rather large roughness of ~10 Å. Interestingly, the crucial $C_{60} \rightarrow$ Cu and Cu $\rightarrow C_{60}$ interfaces that produce the long-range magnetic order in the samples are much smoother, with a roughness of ~5–6 Å. The decreased interfacial roughness is also apparent in the Au cap layers.

From fitting the neutron data, we can estimate the SLD of the different layers. The neutron SLDs for C_{60} and Cu are in reasonable agreement with the values reported in Table I for the SL sample. We attribute the differences between the two samples primarily to the narrower Q-range for the NR scans for the TL sample as compared to the SL sample. The more limited Q-range permits a wider variation in fitting parameters with equivalent fidelity to the data.

CONCLUSIONS

The origin of long-range magnetic order at interfaces of molecular species and transition metals is an intriguing puzzle. Charge transfer processes are thought to play a significant role, strongly suggesting that the magnetic moments should be localized at or close to the interface. Understanding the degree of localization of magnetic moments to the interface will be a key step in formulating a coherent theory of magnetism in this class of materials. Polarized neutron reflectometry is the most direct method of establishing the length scale of interfacial magnetism,[18–20] and our investigations highlight several considerations for future studies. The interface roughness can be considerable at C_{60}/metal interfaces. However, it is not clear if very smooth interfaces would enhance the magnetism in C_{60}/non-magnetic metal structures or whether the decreased contact area between the two species reduces the overall charge transfer to C_{60}. Some degree of interface roughness may be ideal for the development of a robust interfacial magnetization.

Figure 4 provides another perspective for future studies. The scattering length density profile for the x-ray reflectivity shows a large contrast between the Cu and C_{60} layers, and the x-ray scattering from these layers produces strong superlattice Bragg peaks that increase the intensity of the scattered beam by almost an order of magnitude. This is a crucial feature in looking for a magnetic scattering signal from a weakly magnetized sample. The neutron SLD profile, however, shows much weaker contrast, less than 20%, between the Cu and C_{60} layers. Hence, the superlattice Bragg peak at $Q \sim 0.06$ Å^{-1} clearly visible in the x-ray scan is essentially missing in the neutron data.

The Cu/C_{60} interface is known to produce the most robust long-range spin ordering in C_{60}/transition metal structures. However, other materials that are also known to generate a ferromagnetic state may be better suited for neutron scattering studies. For example, Mn/C_{60} multilayers have a magnetization that is about 3× smaller than the Cu/C_{60} system,[10] but the contrast in neutron

scattering length density may compensate for this effect. Nominal SLD values are $5.5 \times 10^{-6}/Å$ for C_{60}, $6.5 \times 10^{-6}/Å$ for Cu, and $\sim -3 \times 10^{-6}/Å$ for Mn. This large variation in C_{60} and Mn SLD, in both magnitude and sign, should produce strong scattering contrast, generating well-defined superlattice Bragg peaks. As the intensity of the superlattice Bragg peaks can be an order of magnitude or more than that of adjacent regions of reciprocal space, such a structure should allow for the much greater counting statistics required to reveal the contribution from weak magnetic scattering. Polarized neutron scattering studies of such a system would help resolve the crucial question of the interfacial length scale of the long-range magnetic order.

ACKNOWLEDGMENTS

REFERENCES

[1] L. Torsi, M. Magliulo, K. Manoli, and G. Palazzo, "Organic field-effect transistor sensors: A tutorial review," Chem. Soc. Rev. **42**, 8612 (2013).

[2] E. Orgiu and P. Samorì, "25th anniversary article: Organic electronics marries photochromism: Generation of multifunctional interfaces, materials, and devices," Adv. Mater. **26**, 1827–1845 (2014).

[3] T. D. Nguyen, E. Ehrenfreund, and Z. V. Vardeny, "Spin-polarized light-emitting diode based on an organic bipolar spin valve," Science **337**, 204–209 (2012).

[4] M. P. de Jong, "Recent progress in organic spintronics," Open Phys. **14**, 337–353 (2016).

[5] S. Delprat, M. Galbiati, S. Tatay, B. Quinard, C. Barraud, F. Petroff, P. Seneor, and R. Mattana, "Molecular spintronics: The role of spin-dependent hybridization," J. Phys. D: Appl. Phys. **51**, 473001 (2018).

[6] R. A. Cheville and N. J. Halas, "Time-resolved carrier relaxation in solid C_{60} thin films," Phys. Rev. B **45**, 4548–4550 (1992).

[7] H. Liu, J. Wang, M. Groesbeck, X. Pan, C. Zhang, and Z. V. Vardeny, "Studies of spin related processes in fullerene C_{60} devices," J. Mater. Chem. C **6**, 3621–3627 (2018).

[8] K.-D. Tsuei, J.-Y. Yuh, C.-T. Tzeng, R.-Y. Chu, S.-C. Chung, and K.-L. Tsang, "Photoemission and photoabsorption study of C_{60} adsorption on Cu(111) surfaces," Phys. Rev. B **56**, 15412–15420 (1997).

[9] M. Gobbi, F. Golmar, R. Llopis, F. Casanova, and L. E. Hueso, "Room-temperature spin transport in C_{60}-based spin valves," Adv. Mater. **23**, 1609–1613 (2011).

[10] F. A. Ma'Mari, T. Moorsom, G. Teobaldi, W. Deacon, T. Prokscha, H. Luetkens, S. Lee, G. E. Sterbinsky, D. A. Arena, D. A. MacLaren, M. Flokstra, M. Ali, M. C. Wheeler, G. Burnell, B. J. Hickey, and O. Cespedes, "Beating the Stoner criterion using molecular interfaces," Nature **524**, 69–73 (2015).

[11] J. Ma, C. Liu, and K. Chen, "Assembling non-ferromagnetic materials to ferromagnetic architectures using metal-semiconductor interfaces," Sci. Rep. **6**, 34404 (2016).

[12] T. Lan Anh Tran, D. Çakır, P. K. Johnny Wong, A. B. Preobrajenski, G. Brocks, W. G. van der Wiel, and M. P. de Jong, "Magnetic properties of bcc-Fe(001)/C 60 interfaces for organic spintronics," ACS Appl. Mater. Interfaces **5**, 837–841 (2013).

[13] J. A. Dura, D. J. Pierce, C. F. Majkrzak, N. C. Maliszewskyj, D. J. McGillivray, M. Lösche, K. V. O'Donovan, M. Mihailescu, U. Perez-Salas, D. L. Worcester, and S. H. White, "AND/R: Advanced neutron diffractometer/reflectometer for investigation of thin films and multilayers for the life sciences," Rev. Sci. Instrum. **77**, 074301 (2006).

[14] J. R. P. Webster, S. Langridge, R. M. Dalgliesh, and T. R. Charlton, "Reflectometry techniques on the second target station at ISIS: Methods and science," Eur. Phys. J. Plus **126**, 112 (2011).

[15] G. P. Flecher and J. F. Anker, "Polarized-neutron reflectometry," J. Magn. Magn. Mater. **200**, 741–754 (1999).

[16] C. Elschner, A. A. Levin, L. Wilde, J. Grenzer, C. Schroer, K. Leo, M. Riede, and IUCr, "Determining the C_{60} molecular arrangement in thin films by means of X-ray diffraction," J. Appl. Crystallogr. **44**, 983–990 (2011).

[17] B. J. Kirby, P. A. Kienzle, B. B. Maranville, N. F. Berk, J. Krycka, F. Heinrich, and C. F. Majkrzak, "Phase-sensitive specular neutron reflectometry for imaging the nanometer scale composition depth profile of thin-film materials," Curr. Opin. Colloid Interface Sci. **17**, 44–53 (2012).

[18] C. F. Majkrzak, K. V. O'Donovan, and N. F. Berk, "Polarized neutron reflectometry," Neutron Scattering Magn. Mater. **2006**, 397–471.

[19] M. R. Fitzsimmons and C. F. Majkrzak, "Application of polarized neutron reflectometry to studies of artificially structured magnetic materials," in *Modern Techniques for Characterizing Magnetic Materials* (Kluwer Academic Publishers, 2005), pp. 1–52.

[20] M. R. Fitzsimmons, S. D. Bader, J. A. Borchers, G. P. Felcher, J. K. Furdyna, A. Hoffmann, J. B. Kortright, I. K. Schuller, T. C. Schulthess, S. K. Sinha, M. F. Toney, D. Weller, and S. Wolf, "Neutron scattering studies of nanomagnetism and artificially structured materials," J. Magn. Magn. Mater. **271**, 103–146 (2004).